Contents lists available at ScienceDirect

Earth and Planetary Science Letters

Late Carboniferous paleoelevation of the Variscan Belt of Western Europe

Camille Dusséaux [a],[*], Aude Gébelin [a], Gilles Ruffet [b],[c], Andreas Mulch [d],[e]

[a] *SoGEES, University of Plymouth, PL48AA Plymouth, UK*
[b] *CNRS (CNRS/INSU) UMR 6118, Géosciences Rennes, 35042 Rennes Cedex, France*
[c] *Université de Rennes 1, Géosciences Rennes, 35042 Rennes Cedex, France*
[d] *Senckenberg Biodiversity and Climate Research Centre (SBiK-F), 60325 Frankfurt, Germany*
[e] *Institute of Geosciences, Goethe University Frankfurt, 60438 Frankfurt, Germany*

A R T I C L E   I N F O

A B S T R A C T

We present the first stable isotope paleoaltimetry estimates for the hinterland of the eroded Variscan Belt of Western Europe based on the hydrogen isotope ratios of muscovite from syntectonic leucogranites that have been emplaced at ∼315 Ma. We focus on the Limousin region (Western Massif Central, France) where peraluminous granites are spatially associated with strike-slip and detachment shear zones that developed as a consequence of Late Carboniferous syn- to post-orogenic extension. In this region, we show that the north-east corner of the Millevaches massif (located at the junction between brittle and ductile fault systems) represented a pathway for Earth surface-derived fluids that penetrated the crust and reached the ductile segment of the low-angle Felletin detachment zone. Using microstructural, thermometry, hydrogen isotope and $^{40}Ar/^{39}Ar$ geochronological data, we show that these Variscan meteoric fluids interacted with hydrous silicates during high temperature deformation between ∼318 and 310 Ma. For paleoaltimetry purposes, we reference our hydrogen isotope record (δD) of ancient meteoric fluids from mylonitic rocks to ∼295 Myr-old records retrieved from freshwater shark remains preserved in the Bourbon l'Archambault basin that developed in the external zones of the orogen. A ∼76‰ difference in $\delta D_{meteoric\ water}$ values between the Millevaches massif ($\delta D_{meteoric\ water}$ value = -96 ± 8‰) and the Bourbon l'Archambault foreland basin (δD_{water} value = -20 ± 6‰) is consistent with paleoaltimetry estimates of 3.4 ± 0.7 km based on a modern lapse rate of ∼-22‰/km for δD_{water} values. The rather large difference in δD values between the foreland basin and the continental interior suggests that the hinterland of the Variscan belt of western Europe was high enough to act as a barrier to moisture transport from the south-south-east and induce an orographic rain shadow to the north.

© 2021 Elsevier B.V. All rights reserved.

1. Introduction

The Variscan belt, extending from South America to East Asia through North America and Central Europe, is a Himalayan-type collision belt that resulted from protracted convergence between the Laurentia-Baltica and Gondwana lithospheric plates between ∼410 and ∼310 Ma (e.g. Matte, 2001). This extensive mountain belt exposes vast amounts of granites, migmatitic complexes and granulite facies rocks and is considered a "hot orogen" characterized by crustal thickening, syntectonic crustal melting, high-grade metamorphism, and syn- to post-convergence gravitational collapse (Fig. 1; e.g. Gébelin et al., 2009; Vanderhaeghe et al., 2020).

The paleotopography of the Variscan orogen has been the focus of considerable debate with estimates ranging from ∼2000 to ∼5000 m (e.g. Dörr and Zulauf, 2010; Franke, 2014). Principally, two competing models have been proposed: 1) a Himalaya-Tibet style high orogenic plateau that developed as a result of thickened hinterland regions (e.g. Becq-Giraudon et al., 1996; Dörr and Zulauf, 2010; Goddéris et al., 2017), and 2) subdued topography due to coeval orogen-parallel extension that counterbalanced crustal thickening and surface uplift (e.g. Roscher and Schneider, 2006; Franke, 2014). Therefore, assessing the paleoaltitude of this mountain chain is critical to distinguish between these two models.

Quantifying the topographic evolution of the Variscan belt is also of capital importance to understanding its impact on past global climate change as the Late Carboniferous-Permian transition represents a period of climatic upheaval (Montañez and Poulsen, 2013). By analogy with the modern Himalayan-Tibetan
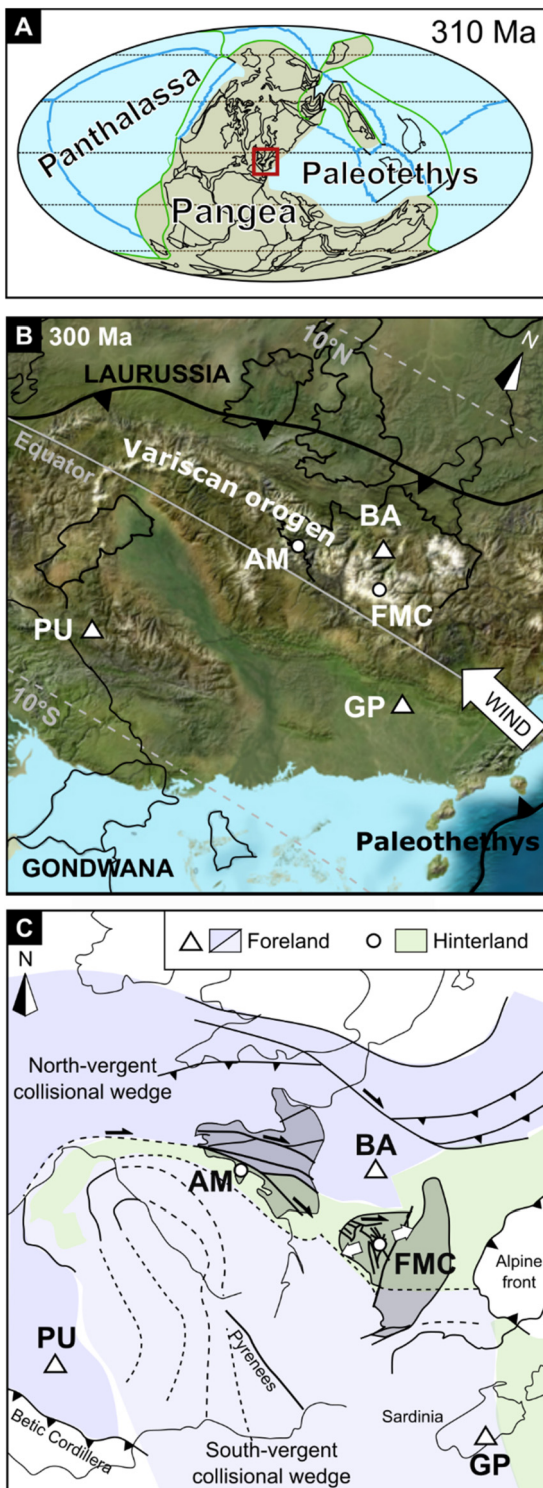
Fig. 1. (A) Late Carboniferous paleogeographic map (after Domeier and Torsvik, 2014). Red square indicates location of the study area in B. (B) Late Carboniferous paleogeographic map modified after Blakey (2011; downloaded in 2016). Modelled moisture transport direction is indicated by a white arrow (Tabor and Poulsen, 2008). (C) Simplified geological map of the Variscan belt of Western Europe modified after Franke et al. (2017) and Rubio Pascual et al. (2016). White circles and triangles indicate the location of our hinterland (syntectonic muscovite, this study) and foreland proxy records (freshwater shark teeth and spines; Fischer et al., 2013), respectively. AM: Armorican Massif, FMC: French Massif Central, PU: Puertollano basin, BA: Bourbon l'Archambault basin, and GP: Guardia Pisano basin. (For interpretation of the colours in the figure(s), the reader is referred to the web version of this article.)

orogen strengthening the modern Asian Monsoon climate (Boos and Kuang, 2010), global and local climate variability would have been majorly impacted by the elevation changes of the Central Pangean (Appalachian-Variscan) mountain belt (e.g. Fluteau et al., 2001). However, no quantification of Paleozoic surface topography has been obtained to date for the Variscan orogen.

Here, we use stable isotope paleoaltimetry, a technique that recovers the isotopic composition of ancient rainwater which scales in a predictable fashion with elevation (e.g. Poage and Chamberlain, 2001), with the aim of quantifying paleoelevation of the hinterland of the Variscan belt of Western Europe during the Late Carboniferous. However, assessing paleoelevation of this fully eroded mountain belt is challenging because the proxies commonly used to reconstruct the topography of orogens (e.g. lacustrine and pedogenic carbonates, volcanic glasses) are absent or altered. Here, we present the first paleoaltimetry estimates for the Variscan belt based on the hydrogen isotope ratios of ancient precipitation retrieved from the low δD values of synkinematic muscovite ($\delta D_{Ms} \leq -90‰$) that crystallized at ~315 Ma in the footwall of extensional shear zones in the continental interior of the orogen.

2. Methods

2.1. Stable isotope paleoaltimetry of eroded orogens

δD values of meteoric fluids can be retrieved from minerals that crystallize during high-temperature deformation in active shear zones infiltrated by surface fluids. Shear zone-based paleoaltimetry has been applied to reconstruct the topography of e.g. the Cenozoic western United States (e.g. Mulch et al., 2007; Gébelin et al., 2012) and the Miocene Himalaya (Gébelin et al., 2013). It is based on the concept that hydrous (shear zone) minerals crystallize in equilibrium with surface-derived, meteoric water. In this study, we use muscovite as a paleoaltimetry proxy because of its 1) high resistance to post-deformational alteration and low-temperature hydrogen isotope exchange, and 2) ability to directly record the timing of mineral formation and isotopic exchange through e.g. $^{40}Ar/^{39}Ar$ geochronology (e.g. Mulch et al., 2005). However, δD values extracted from synkinematic silicates represent maximum values for meteoric fluids, thus minimum paleoelevation estimates, because fluid compositions may be shifted to less negative values at depth due to fluid-rock interaction that occurs during the downward flow of fluids (e.g. Taylor, 1977; Gébelin et al., 2012, 2013). As shown in previous studies of extensional detachment systems, penetration of surface-derived fluids down to the brittle-ductile transition is typically supported by the presence of a large hydraulic head, a porous and permeable upper crust, and a high heat flux sourced by granite and migmatite emplacement in the middle and lower crust, essential to sustain fluid circulation within the top of the active detachment footwall (e.g. Person et al., 2007; Gébelin et al., 2015, 2017; Dusséaux et al., 2019).

Single-site paleoaltimetry reconstructions suffer from uncertainties around paleoclimatic boundary conditions, especially in deep time applications. One approach to resolve climatically induced biases in stable isotope paleoaltimetry (Mulch, 2016, and references therein) is to compare high-elevation stable isotope records (herein from the hinterland of the Variscan belt of western Europe) to climate-controlled records near sea level (herein freshwater shark remains).

2.2. Retrieving the isotope composition of meteoric water in the hinterland

2.2.1. Sampling strategy

Syntectonic leucogranites were first sampled at regional scale within strike-slip and detachment shear zones to determine the
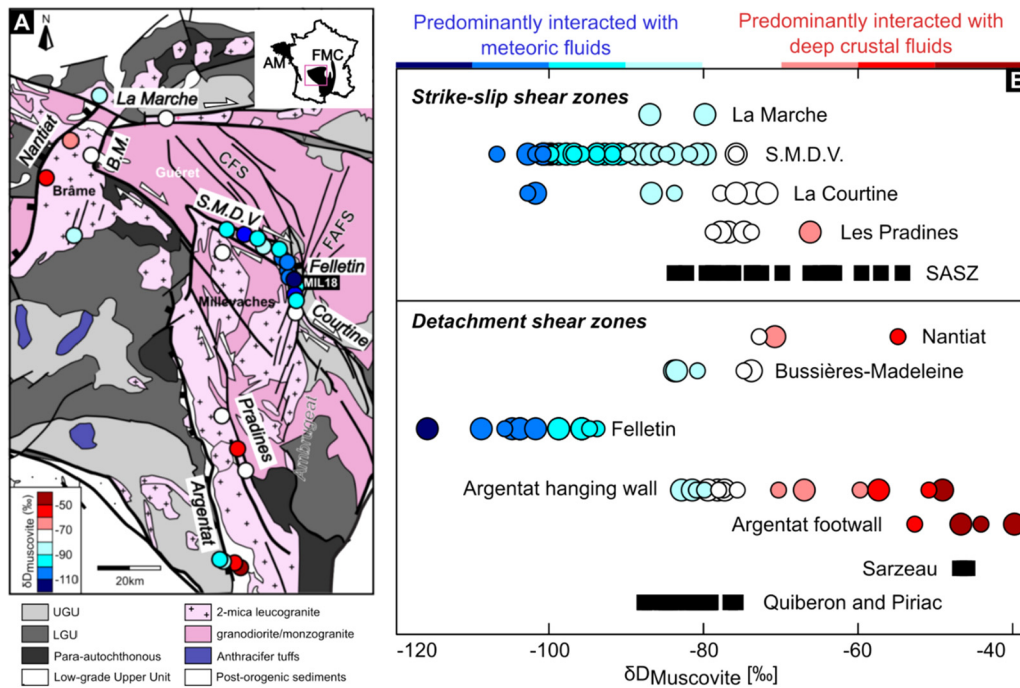
Fig. 2. (A) Geological map of the Limousin (western part of the French Massif Central) indicating sampling sites and results from hydrogen isotope ratios of synkinematic muscovite (δD_{Ms}). (B) δD_{Ms} values obtained on syntectonic leucogranites, quartz veins and pegmatites from strike-slip and detachment shear zones in the Limousin (circles, this study) and Armorican Massif (black squares, Dusséaux et al., 2019). Small circle: 250 < Ms fraction < 500 μm; large circle: Ms fraction > 500 μm; AM: Armorican Massif; FMC: French Massif Central; BM: Bussières-Madeleine; SMDV: Saint-Michel-de-Veisse; CFS: Creuse Fault System; FAFS: Felletin-Ambrugeat Fault System; SASZ: South Armorican Shear Zone (see text for interpretation).

overall pattern of fluid compositions from the hydrogen isotope ratio of muscovite (δD_{Ms}; Fig. 2). Based on preliminary results (δD_{Ms} values < −90‰), specific sites were subsequently targeted to gain a representative range of hydrogen isotopic compositions for the meteoric fluids that permeated these shear zones.

Samples from detachment zones were collected based on their structural position from the hanging wall/footwall interface into the mylonitic footwall. Poor outcrop conditions precluded observation of the hanging wall contact and samples were instead collected most proximally to the detachment interface. Additional sample collection included micaschist and orthogneiss (from the host rocks), as well as pegmatites and muscovite-rich quartz veins (either found parallel to the granite foliation, filling brittle fractures and/or lining fault surfaces that formed in the hanging wall, Fig. 3).

For the stable isotope paleoaltimetry reconstruction, we focused on samples from the northeast corner of the Millevaches massif where especially low δD_{Ms} values provide strong evidence for interaction with meteoric fluids. We particularly targeted the low-angle Felletin detachment zone that forms the roof of the leucogranites (Fig. 2A).

2.2.2. Structural and petrostructural analysis

Structural features, including measurements of foliation planes and lineation direction, were described in detail from a continuous section (Fig. 3A) into the mylonitic footwall of the Felletin detachment shear zone, from mylonitic leucogranite at the top (MIL19 – 0 m) to undeformed leucogranite at the bottom (MIL18I – 90 m). Thin sections were systematically cut parallel to the lineation and perpendicular to the foliation to determine the sense of shear. Micromorphological investigations of muscovite microstructures were performed to characterize the mechanisms of deformation and fluid flow history.

2.2.3. Hydrogen isotope geochemistry

To determine the isotopic composition of meteoric fluids that penetrated the Felletin detachment footwall, we 1) measured the hydrogen isotope ratios of muscovite (Text SM1; Table SM1), 2) deduced an average temperature of hydrogen isotope exchange using the titanium-in-muscovite geothermometer (Text SM2, Table SM2; Wu and Chen, 2015), and 3) used the hydrogen isotope muscovite-water fractionation factor of Suzuoki and Epstein (1976) (Table 1).

2.2.4. Ar/Ar geochronology

To constrain the timing and duration of recrystallization and fluid flow in the hydrothermal system, five muscovite single grains from mylonitic leucogranite samples MIL19, MIL18C, MIL18D, MIL18H and MIL18I were laser step-heated for $^{40}Ar/^{39}Ar$ geochronology (Fig. 3D; Text SM3; Tables SM3 and SM4).

2.3. Retrieving the isotope composition of meteoric water in the low-elevation foreland: the Bourbon l'Archambault basin

For our stable isotope paleoaltimetry reconstruction, we reference the hydrogen isotope record from the elevated Variscan hinterland (new data herein) to low-elevation oxygen isotope records from teeth and spines of two freshwater shark species preserved in the Bourbon l'Archambault basin (Fischer et al., 2013; Fig. 1B, Fig. SM2, Table 2). The phosphate-oxygen bond in shark teeth fluorapatite is very resistant to diagenetic alteration, thus representing a reliable low-elevation proxy. The Bourbon l'Archambault basin is situated close to our study area (~100 km from the hinterland sites) and developed close to sea level in the external zones of the orogen (Fischer et al., 2013). Sedimentological, paleogeographical, ecological and geochemical ($\delta^{18}O_P$ and $^{87}Sr/^{86}Sr$ values; Table 2) data from previous studies indicate that the sharks evolved in a freshwater environment (lacustrine to fluvial; Fischer et al., 2013). The sedimentary record has been biostratigraphically and isotopically dated as Sakmarian in age (~295 to 290 Ma; e.g. Roscher
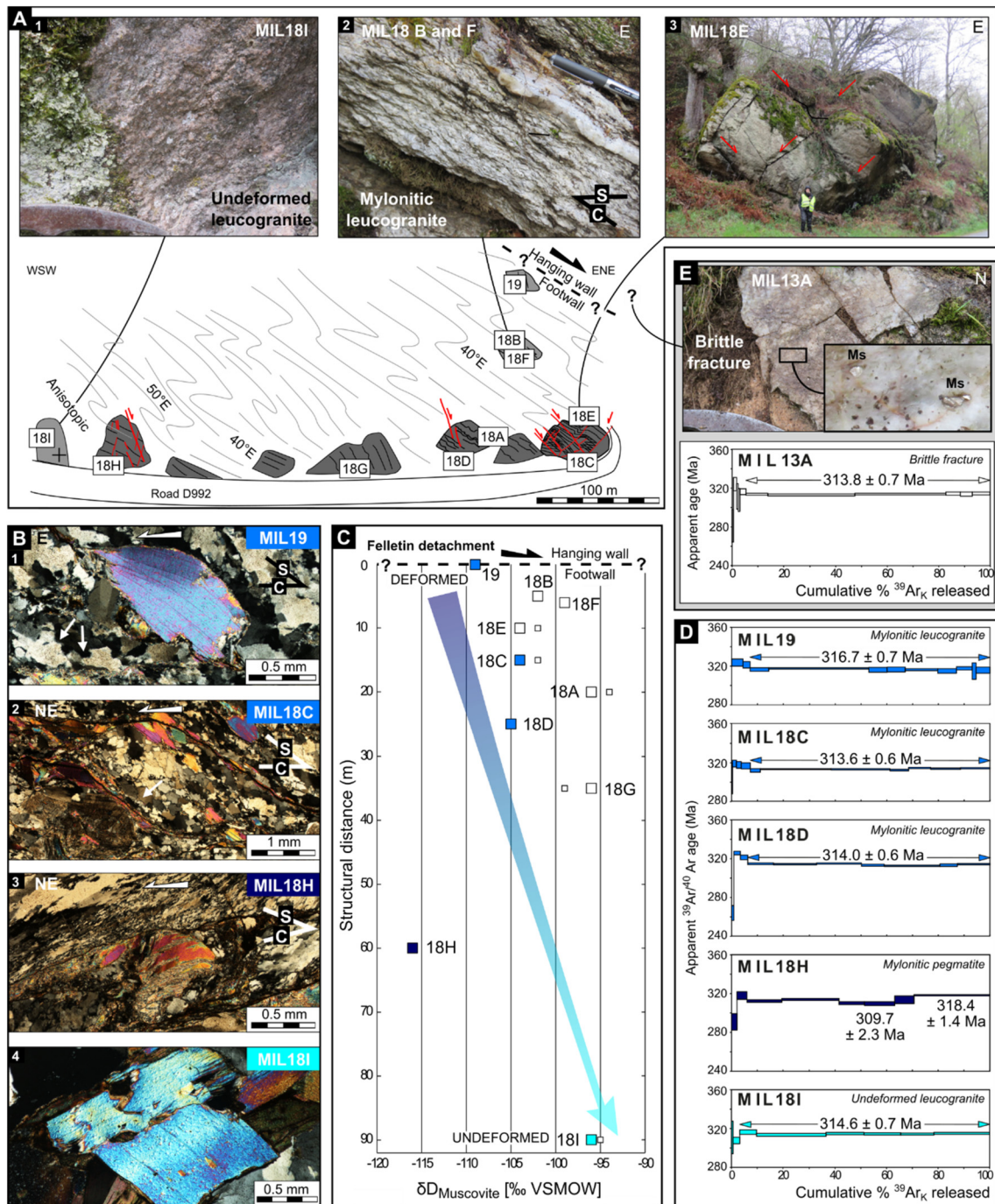
Fig. 3. (A) Felletin detachment footwall outcrop description (Millevaches massif, French Massif Central) showing location of studied samples. (B) Microstructure photographs of analyzed samples: (B1) Lenticular muscovite fish and quartz grains highlighting castellate boundaries (white arrows), (B2) Muscovite fish forming C-S structures and quartz showing grain-boundary migration, (B3) ultramylonitic facies displaying recrystallization of tiny muscovite grains within shear planes from primary muscovite and quartz recrystallization by subgrain rotation, (B4) euhedral muscovite grains in undeformed leucogranite. (C) Hydrogen isotope ratios of muscovite (δD_{Ms} values; small squares: 250 $<$ Ms fraction $<$ 500 µm; large squares: Ms fraction $>$ 500 µm) plotted against the estimated structural distance to the hanging wall (0 to 90 m). Note that point 18H does not follow a linear trend of increasing δD_{Ms} values with increasing distance to the detachment. (D) $^{40}Ar/^{39}Ar$ step-heating spectra (1σ) on single muscovite grains from leucogranite and pegmatite. (E) $^{40}Ar/^{39}Ar$ step-heating spectra (1σ) on single muscovite grains that crystallized on brittle fault plane and associated outcrop photograph. Samples analyzed in (D) are shown in blue colors in (B) and (C). See text for explanations.

Table 1

δD_{water} values and uncertainties calculated using the temperatures of muscovite-water hydrogen isotope exchange obtained from the Ti-in-Ms geothermometer (Wu and Chen, 2015), the measured δD_{Ms} values from syntectonic leucogranites emplaced in the Felletin detachment footwall (NE corner of the Millevaches massif) and the hydrogen isotope fractionation factor of Suzuoki and Epstein (1976). Grey lines indicate data used for paleoaltimetry reconstruction.

Sample	Distance (m)	Rock type	δD_{Ms} (‰ VSMOW)	Uncertainty (‰)	Fraction Ms (μm)	T (°C)	Uncertainty (°C)	δD_{water} (‰ VSMOW)	-	+
MIL19	0	Mylonitic leucogranite	−109	2	500<f	540	51	-95	-4	5
MIL18B	5	Mylonitic leucogranite	−102	2	500<f	540	51	-88	-4	5
MIL18F	6	Quartz vein	−99	2	500<f	540	51	-85	-4	5
MIL18E	10	Mylonitic leucogranite	−104	2	500<f	540	51	-90	-4	5
MIL18C	15	Mylonitic leucogranite	−104	2	500<f	493	57	-86	-5	8
MIL18A	20	Mylonitic leucogranite	−96	2	500<f	540	51	-82	-4	5
MIL18D	25	Mylonitic leucogranite	−105	2	500<f	540	51	-91	-4	5
MIL18G	35	Mylonitic leucogranite	−99	2	250<f<500	540	51	-85	-4	5
MIL18H	60	Mylonitic pegmatite	−116	2	500<f	568	42	-104	-3	3
MIL18I	90	Undeformed leucogranite	−96	2	500<f	559	55	-83	-4	5
AVERAGE of MIL19, MIL18D and MIL18H			**-110**					**-96**	**-4**	**4**
SD			6					7	1	1
Min			−116					-104	−3	3
Max			−105					-91	−4	5

and Schneider, 2005), and shark teeth have not been affected by diagenetic alteration resulting in well preserved bioapatite (Fischer et al., 2013). Nine Lissodus and seven Orthacanthus spines provide $\delta^{18}O_P$ values that range from 15.5 to 17.6‰ (n=17) and $^{87}Sr/^{86}Sr$ ratios from 0.71058 to 0.71077 (n=4). Data from these lifelong proxies are similar to those obtained on Orthacanthus tooth enameloid that yields a $\delta^{18}O_P$ value of 16.6‰ and an $^{87}Sr/^{86}Sr$ ratio of 0.71061.

2.4. Lapse rate used for paleoaltimetry reconstructions

In contrast to most stable isotope paleoaltimetry studies conducted in ancient orogens located in mid to low latitudes, our study focuses on an eroded mountain chain for which paleomagnetic data (e.g. Edel et al., 2018) indicate that it straddled the Equator during the Carboniferous (Fig. 1; e.g. Domeier and Torsvik, 2014; Kent and Muttoni, 2020). Here, we use the empirical isotope-elevation relationship (Poage and Chamberlain, 2001) for global low-to-mid latitude mountain belts in order to estimate a Variscan paleoelevation.

However, this relationship between elevation and the δD and $\delta^{18}O$ values of precipitation must be applied with caution. When comparing with present-day conditions, three parameters may have changed the isotopic lapse rate over the Pangean mountains during the late Carboniferous. The presence of an Intertropical Convergence Zone, typical of tropical regions, may have caused monsoonal precipitation and rising air masses, and, by controlling the spatiotemporal distribution of precipitation and consequently the isotopic composition, may have led to a reduced lapse rate when compared to higher latitudes (e.g. Poulsen et al., 2007; Heavens et al., 2015). Two important glacial periods at ~315 and ~295 Ma concomitant with the timing of proxy formation suggests that the Pangean domain was likely characterized by rather cold and arid conditions. When compared to modern observations, globally cooled conditions may have increased the lapse rate over high altitudes (~5000 m; e.g. Poage and Chamberlain, 2001; Heavens et al., 2015; Kent and Muttoni, 2020). Global temperatures during the Late Carboniferous may have been up to 10°C cooler than modern temperatures (Feulner, 2017). Hence, simple Rayleigh distillation under glacial temperatures is expected to result in lower paleoaltitude estimates; an effect that may account for lowering of calculated paleoelevations on the order of 5-20% (Rowley, 2007).

Here, we calculate paleoelevation of the Variscan belt of Western Europe using a lapse rate defined for mid to low latitudes (−2.8‰/km for $\delta^{18}O$ and −22‰/km for δD; Poage and Chamberlain, 2001). However, considering the equatorial paleogeographic context, this lapse rate underestimates paleoaltimetry estimates when compared to present-day tropical lapse rates (−1.8‰/km for $\delta^{18}O$ and −14.6‰/km for δD; Saylor et al., 2009).

3. Hinterland data: western part of the French Massif Central

3.1. Geological background

The focus of this study is on the Limousin region (Western part of the French Massif Central) where syntectonic granites are spatially associated with major detachment and strike-slip shear zones. The Limousin is part of the hinterland of the West European Variscan collisional belt that shows a range of tectono-metamorphic events (~360–310 Ma) from crustal thickening and associated Barrovian metamorphism to lithospheric thinning accommodated by regional-scale strike-slip shear zones and low-angle detachment zones (e.g. Matte, 2001; Gébelin et al., 2009; Vanderhaeghe et al., 2020). Here, the end of the orogeny (~320 to 300 Ma) is characterized by high-grade metamorphism and syntectonic leucogranites emplacement within crustal-scale shear zones

Table 2

$\delta^{18}O_{water}$ values and uncertainties calculated using a paleotemperature of 29 ± 3‰ (Dera et al., 2009; Fischer et al., 2013), the $\delta^{18}O_P$ values of shark teeth and spines (Fischer et al., 2013) preserved in the foreland Bourbon l'Archambault basin and the phosphate-water fractionation factor of Lécuyer et al. (2013). Grey lines indicate data used for paleoaltimetry reconstruction.

Locality	Formation	Age	Taxon	Sample	Material	$\delta^{18}O_P$ (‰ VSMOW)	$^{87}Sr/^{86}Sr$	T (°C)	± (°C)	$\delta^{18}O_{water}$ (‰ **VSMOW**)	± (°C)
Bourbon l'Archambault Basin (France)	Buxières Fm	Early Permian, Sakmarian (295 - 290 Ma)	*Lissodus*	LBS 1A	fin spine	16.7	0.71070	29	3	**-2.9**	0.7
				LBS 1B	fin spine	16.9		29	3	**-2.8**	0.7
				LBS 2	fin spine	16.4	0.71058	29	3	**-3.2**	0.7
				LBS 2A	fin spine	16.6		29	3	**-3.1**	0.7
				LBS 2B	fin spine	16.7		29	3	**-2.9**	0.7
				LBS 2C	fin spine	16.7		29	3	**-3.0**	0.7
				LBS 3	fin spine	15.6	0.71077	29	3	**-4.0**	0.7
				LBS 3A	fin spine	16.0		29	3	**-3.7**	0.7
				LBS 3B	fin spine	15.5		29	3	**-4.1**	0.7
			Orthacanthus buxieri	OB1	tooth enameloid	16.6	0.71061	29	3	**-3.1**	0.7
				OBS 1a	dorsal spine	16.6		29	3	**-3.0**	0.7
				OBS 2a	dorsal spine	16.3		29	3	**-3.4**	0.7
				OBS 1b	dorsal spine	16.0		29	3	**-3.6**	0.7
				OBS 2b	dorsal spine	16.7		29	3	**-2.9**	0.7
				OBS 3b	dorsal spine	17.6		29	3	**-2.1**	0.7
				OBS 4b	dorsal spine	17.4		29	3	**-2.2**	0.7
				OBS 5b	dorsal spine	16.4		29	3	**-3.3**	0.7
					Average of LBS3, LBS3A, LBS3B, OBS2A and OBS1B	15.9				**-3.8**	
					SD	0.3				**0.3**	
					Min	15.5				**-4.1**	
					Max	16.3				**-3.4**	

distributed in a flower structure representing the south-east extension of the South Armorican Shear Zone (Fig. 2A; Gébelin et al., 2007, 2009). These Late Carboniferous shear zones were active while this part of the orogen was otherwise collapsing, inducing the development of extensional structures in the internal transpression zones and thrust faults in the external zones (e.g. Gébelin et al., 2007, 2009).

3.2. Stable isotope results at the regional scale

Samples (n=68) of leucogranite, pegmatite, quartz vein, micaschist, and gneiss from ductile shear zones yield muscovite hydrogen isotope ratios (δD_{Ms}) between −116 ± 2‰ to −40 ± 2‰ (Fig. 2; Table SM1). Muscovite from mylonitic leucogranites emplaced within strike-slip shear zones in the northern part of the area (La Marche shear zone) provide δD_{Ms} values ranging from −87 to −80‰ (n=2). In contrast, muscovite from deformed leucogranite further south along the St-Michel-de-Veisse (n=11) and La Courtine (n=2) dextral strike-slip faults provides lower δD_{Ms} values from −107 to −76‰. However, undeformed leucogranites from this southern strike-slip fault network show higher values of −74‰ and −72‰ (n=2). Sheared pegmatites from the same strike-slip shear zones indicate consistently low δD_{Ms} values between −102 and −76‰ (n=12), while quartz veins (n=4) yield constant δD_{Ms} values that range from −87 to −82‰. Higher δD_{Ms} values (−79 to −66‰; n=4) have been measured on syntectonic muscovite from the strike-slip Pradines mylonitic fault in the Millevaches massif.

Perpendicular to the E-W strike-slip shear zone trend, low-angle normal faults bound the Brâme massif (northwest corner of the Limousin region) and the Millevaches massif. The Nantiat detachment that forms the western boundary of the Brâme massif, exposes mylonitic granites that yield δD_{Ms} values ranging from −73 to −55‰ (n=2). Lower δD_{Ms} values from −84 to −74‰ (n=3) are found in the eastern part of the Brâme massif along the Bussières-Madeleine normal fault. The brittle-ductile Argentat normal fault bounds the Millevaches massif to the west and indicates high δD_{Ms} values both in the hanging wall (−83‰ ≤ δD_{Ms}

≤ −49‰ in 8 orthogneiss samples) and the footwall (−49‰ ≤ δD_{Ms} ≤ −40‰ in 4 mica schist samples).

Much lower δD_{Ms} values (−116‰ ≤ δD_{Ms} ≤ −94‰) are found in mylonitic leucogranite (n=9), undeformed leucogranite (n=1), mylonitic pegmatite (n=1) and a quartz vein (n=1) near Felletin (eastern Millevaches massif), at the junction of several brittle (Creuse and Felletin-Ambrugeat) and ductile (St-Michel-de-Veisse and Courtine) fault systems. To the northeast part of the Millevaches granite, brittle normal faults, part of the Felletin-Ambrugeat Fault system, have been sealed by muscovite-rich quartz veins that yield δD_{Ms} values of −87 to −85‰ (MIL13A; Fig. 3E).

In the following, we focus on the Felletin detachment footwall where synkinematic muscovite highlight a strong meteoric fluid signature (δD_{Ms} values as low as −116‰; see discussion).

3.3. Structural outcrop data

Within the top ∼80 m of section in the Felletin mylonitic footwall, deformed two-mica leucogranites display a shallow to moderate (10-30°) ENE-dipping foliation (S plane) and a ∼N025 trending stretching lineation. Syntectonic pegmatites (MIL18H) and quartz veins (MIL18F) are orientated parallel to the mylonitic leucogranite foliation. This foliation is characterized by S-planes making an angle of ∼40° with C-planes marked by muscovite fish. C-S structures at the macroscopic (Fig. 3A-2) and microscopic scale (Fig. 3B-2) largely support a syntectonic leucogranite emplacement with a top-to-the-northeast sense of shear. Top-to-the-southwest sense of shear (indicated by asymmetric feldspar grains with pressure shadows) are also displayed in some samples. Nonetheless, the majority of shear sense indicators such as asymmetric tails and/or shear bands indicate a top-to-the-northeast sense of shear (Figs. 3A-2 and 3B-2).

The entire section is affected by extensional conjugate brittle fractures (Fig. 3A, red arrows) that, as observed to the north along the Felletin-Ambrugeat fault system, dip ∼50° to the ENE and WSW. Along the St Michel-de-Veisse fault (north of the section),

similar fractures are filled by quartz veins containing muscovite (Fig. 3E).

3.4. Petrostructural analysis

Microstructural observations indicate an abundance of mica fish formed by simultaneous grain rotation and reduction of their upper and lower sides and drag along micro shear zones (Fig. 3B-1). Some ultramylonitic facies only show shear bands made of tiny grains that develop as a result of intense shearing and alteration of primary muscovite (Fig. 3B-3). In all studied samples (MIL19 – 0 m, MIL18C – 15 m, MIL18H – 60 m and MIL18I – 90 m), quartz grains show sub-solidus deformation textures such as castellate microstructures indicating that grain boundary migration ($\sim$500 to 700°C; e.g. Stipp et al., 2002) was the dominant dynamic recrystallization process occurring during syntectonic granite emplacement (Fig. 3B-1 and 2). However sub-grain rotation operating at lower temperature ($\sim$400 to 500°C; e.g. Stipp et al., 2002) is also indicated by quartz ribbons of sheared pegmatite with low δD_{Ms} values (MIL18H, $\delta D_{Ms} = -116\permil$; Fig. 3B-3). In contrast, the undeformed granite sample (MIL18I) displays euhedral muscovite grains (Fig. 3B-4) and primary quartz crystals.

3.5. Titanium-in-muscovite thermometry

Three samples have been selected (mylonitic pegmatite MIL18H, $\delta D_{Ms} = -116\permil$; mylonitic leucogranite MIL18C, $\delta D_{Ms} = -104\permil$; and undeformed leucogranite MIL18I, $\delta D_{Ms} = -96\permil$) covering a rather large deformation and strain gradient.

Muscovite grains contain $0.00 < Ti < 0.05$ a.p.f.u, $0.02 < Na < 0.10$ a.p.f.u, $0.04 < Mg < 0.18$ a.p.f.u and $0.08 < Fe < 0.37$ a.p.f.u (Table SM2; Fig. SM1). Compositional profiles indicate chemical zoning of muscovite fish from the inner to the outer part of the grain highlighted by major element compositions and particularly evident for Mg, Fe and Na. From core to rim, we note an increase of up to three times in the Mg content (sample MIL18C zone B; core: Mg = 0.06 a.p.f.u; rim: Mg = 0.18 a.p.f.u) and four times in the Fe content (core: 0.08 a.p.f.u; rim: 0.37 a.p.f.u), and a decrease of up to eight times in the Na content (core: 0.10 a.p.f.u; rim: 0.02 a.p.f.u). Euhedral muscovite grains from the undeformed sample MIL18I do not show any particular compositional zonation and display the same low-Mg ($0.07 < Mg < 0.11$ a.p.f.u), low-Fe ($0.08 < Fe < 0.12$ a.p.f.u) and high-Na ($0.05 < Na < 0.09$ a.p.f.u) composition as the core of muscovite fish in deformed samples.

Using a pressure of 4 ± 1 kbar (Gébelin et al., 2006) and the average chemical composition of muscovite for each individual sample, the geothermometer of Wu and Chen (2015) indicates temperatures of 493 ± 57°C for the mylonitic leucogranite (MIL18C), 568 ± 42°C for the pegmatite (MIL18H) and 559 ± 55°C for the undeformed granite (MIL18I) yielding an average temperature of 540 ± 51°C (Table SM2).

3.6. Hydrogen isotopic composition of fluids in the Felletin footwall

We calculated an average δD_{water} value of $-96 \pm 8\permil$ using a temperature of hydrogen isotope exchange of 540 ± 51°C, the hydrogen isotope muscovite-water fractionation factor of Suzuoki and Epstein (1976) and the average of the lowest 30% of the measured δD_{Ms} values (n=3; MIL18H, $\delta D_{Ms} = -116\permil$; MIL19, $\delta D_{Ms} = -109\permil$; MIL18D, $\delta D_{Ms} = -105\permil$; see Figs. 4A and 4C, Table 1 and discussion below for details and uncertainties).

3.7. $^{40}Ar/^{39}Ar$ Geochronology

Muscovite from the MIL19 (0 m), MIL18C (15 m) and MIL18D (25 m) mylonitic leucogranite samples (Fig. 3D) provide plateau ages (1σ) of 316.7 ± 0.7 Ma, 313.7 ± 0.6 Ma, and 314.0 ± 0.6 Ma, respectively, including more than 90% of total $^{39}Ar_K$ released. The undeformed sample MIL18I (90 m) yields a plateau age of 314.6 ± 0.7 Ma (1σ). A muscovite from the MIL18H syntectonic pegmatite yields a saddle-shaped age spectrum with apparent ages from 318.4 ± 1.4 to 309.7 ± 2.3 Ma. In addition, a single muscovite grain from a brittle fault plane that developed in the hanging-wall provides a plateau age of 313.8 ± 0.7 Ma (1σ) (MIL13A, Fig. 3E).
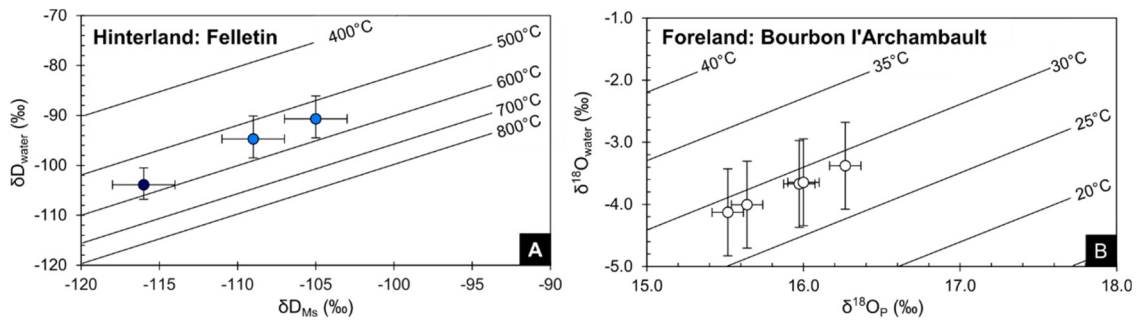
4. Discussion

4.1. Meteoric water-rock interaction in the Felletin detachment footwall

Hydrogen isotope results from the Limousin region reveal a $76\permil$ difference in δD_{Ms} values from values as high as $-40\permil$ indicating a deeper crustal (magmatic/metamorphic) origin ($-80\permil < \delta D_{magmatic\ fluids} < -40\permil$ and/or $-70\permil < \delta D_{metamorphic\ fluids} < -20\permil$; e.g. Field and Fifarek, 1985) to values as low as $-116\permil$ that undeniably reflect a signature of meteoric fluids sourced in either high elevation or high latitude areas (e.g. Mulch, 2016). Intermediate values are interpreted to reflect different degrees of mixing between these two fluid end members. A mixing relationship between meteoric and magmatic/metamorphic fluids has been already established in the southern Armorican domain based on a $42\permil$ difference ($-88\permil \leq \delta D_{Ms} \leq -46\permil$) amongst δD_{Ms} values extracted from Variscan mylonite collected from deep to shallow crustal levels (Dusséaux et al., 2019).

The lowest calculated δD_{water} values ($-104\permil$ to $-82\permil \pm 5\permil$) were obtained in the Felletin detachment footwall (northeast corner of the Millevaches massif). We consider this to represent an exhumed, ancient hydrothermal system that was active during the Late Carboniferous. The structural setting - at the junction between major ductile and brittle fault systems - provides the opportunity for protracted pathways for the downward penetration of surface-derived fluids to the brittle-ductile transition.

D-depleted mica fish along shearing planes interacted with meteoric fluids during high temperature deformation as indicated by quartz microstructures ($\sim$400 to 700°C; Fig. 3B) and the titanium-in-muscovite thermometer (540 ± 51°C; Table SM2, Fig. SM1). This dataset agrees with previous electron backscatter diffraction (EBSD) data obtained on recrystallized quartz ribbons from similar samples that revealed plastic deformation dominated by prismatic <a> glide which occurs between 400 and 700°C (Gébelin et al., 2007).

$^{40}Ar/^{39}Ar$ ages obtained on the same muscovite range from 318.4 ± 1.4 Ma to 309.7 ± 2.3 Ma, in agreement with Late Carboniferous $^{40}Ar/^{39}Ar$ ages ($\sim$325 to 305 Ma) of kinematically equivalent mylonitic rocks from the same and/or surrounding areas interpreted to reflect recrystallization ages from synmagmatic muscovite during leucogranite cooling (e.g. Gébelin et al., 2007, 2009). Based on the rapid cooling that followed the Millevaches granite syntectonic emplacement at 313 ± 4 Ma within the dextral strike-slip Pradines shear zones (Gébelin et al., 2009) and protracted extensional shearing observed in the Felletin area at the roof of Millevaches leucogranites through the brittle-ductile transition (Fig. 3A), ages of 316.7 ± 0.7 Ma (MIL 19, $\delta D_{Ms} = -109\permil$), 314.0 ± 0.6 Ma (MIL 18D, $\delta D_{Ms} = -105\permil$) and 313.6 ± 0.6 Ma (MIL 18C, $\delta D_{Ms} = -104\permil$) are interpreted to reflect the timing of detachment activity during meteoric fluid infiltration. This interpretation is strengthened by microstructural observations supporting mica fish recrystallization by solution-precipitation processes (Fig. 3B), and by the chemical zonation of muscovite fish indicating high Mg and Fe, and low Na contents in their rims in contrast to their cores (EPMA data; Fig. SM1; Table SM2). This core-rim contrast has been correlated with deuterium depletion of syntectonic
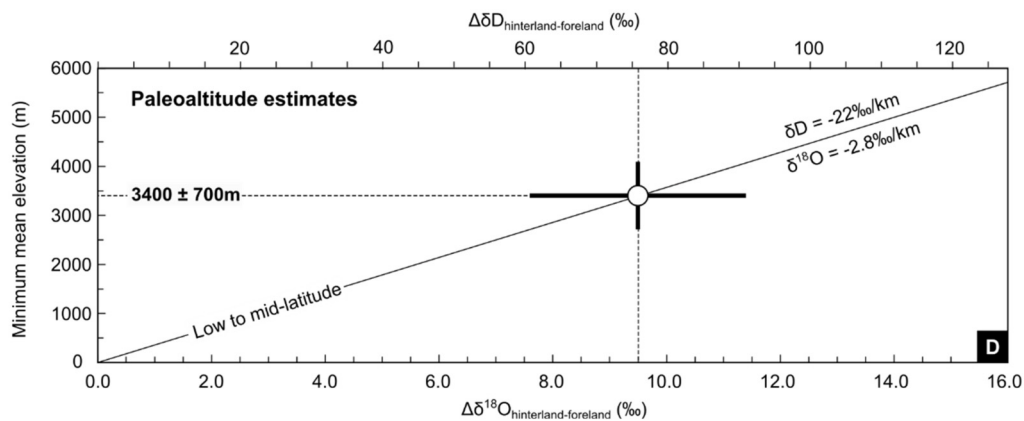
Fig. 4. Uncertainties on the δD_{water} and $\delta^{18}O_{water}$ values used for paleoaltimetry estimate calculations provided in (A) for the hinterland regions using the hydrogen isotope composition of synkinematic muscovite (δD_{Ms}; n=3), the temperatures of water-muscovite isotope exchange deduced from the titanium-in-muscovite geothermometer of Wu and Chen (2015) and the hydrogen isotope muscovite-water fractionation factor of Suzuoki and Epstein (1976), and in (B) for the foreland areas using the oxygen isotope composition of phosphate from shark teeth and spine ($\delta^{18}O_P$; n=5), a temperature of water-phosphate isotope exchange of 29 ± 3°C deduced from modern and Jurassic euryhaline sharks (Dera et al., 2009; Fischer et al., 2013) and the hydrogen isotope phosphate-water fractionation factor of Lécuyer et al. (2013). (C) Table showing converted values from δD_{water} to $\delta^{18}O_{water}$ values (and vice-versa) using the meteoric water line of Craig (1961). (D) Paleoaltitude estimates for the Variscan hinterland of Western Europe and associated uncertainties calculated for low and mid latitude (Poage and Chamberlain, 2001).

muscovite fish and often interpreted to reflect hydrothermal alteration in syntectonic leucogranite (e.g. Miller et al., 1981; Gébelin et al., 2011). Also, euhedral and unzoned muscovite from undeformed samples (see EPMA data of sample MIL18I) present similar chemical compositions than those observed in the cores of depleted micafish, reinforcing the interpretation that meteoric fluid interaction impacted muscovite chemistry. Therefore, we interpret muscovite fish zonation in deformed samples as resulting from muscovite syntectonic recrystallisation by dissolution-precipitation in presence of meteoric fluids.

Ages of 318.4 ± 1.4 Ma and 309.7 ± 2.3 Ma suggested by the saddle shaped age spectrum yielded by muscovite from the syntectonic pegmatite (MIL 18H, $\delta D_{Ms} = -116‰$) indicate partial recrystallization as late as ∼310 Ma (e.g. Alexandrov et al., 2002) and may represent the upper and lower bounds of extensional ductile shearing, respectively.

Muscovite from the undeformed leucogranite sample MIL18I collected at the bottom of the detachment section (Fig. 3) yields an ^{40}Ar/^{39}Ar age of 314.6 ± 0.7 Ma. The same muscovite provided higher δD_{Ms} values of $-96‰$ that, compared to lower values obtained on sheared leucogranite samples suggesting a meteoric fluid-rock exchange during deformation-induced recrystallization, could indicate a lower meteoric fluid/rock ratio and/or a magmatic fluid signature. In agreement with its structural level (90 m from sample MIL19), euhedral shape, and magmatic composition (low-Mg, low-Fe, high-Na), this undeformed muscovite sample remained unaffected by extensional deformation and likely had no interaction with meteoric fluids. Therefore, we consider that the undeformed muscovite from the MIL18I sample recorded cooling below the isotopic closure temperature of muscovite (∼$400 \pm 50°$C) at ∼315 Ma.

Interestingly, muscovite that recrystallized on a fault plane (MIL13A) in the upper crust provides an ^{40}Ar/^{39}Ar age of 313.8 ± 0.7 Ma which is comparable to those obtained on mica fish from syntectonic granite emplaced in the Felletin detachment footwall. This muscovite ^{40}Ar/^{39}Ar plateau age corresponds with relative chronology indicating a start for movement along the N020-striking Felletin-Ambrugeat Fault System at ∼315 Ma (e.g. Cartannaz et al., 2007), demonstrating coeval extension in both the upper and lower crust at ∼315 Ma. In addition, U/Pb data indicate that syntectonic leucogranite emplacement along the Pradines dextral strike-slip shear zone and migmatization of the lower crust also occurred at ∼315 Ma in the center of the Millevaches massif (Gébelin et al., 2009). As suggested for the western part of the French Massif Central (e.g. Burg et al., 1994; Gébelin et al., 2009), these geochronological results reinforce the idea that late Variscan tectonics were characterized by coeval transpression and extension. Importantly, the consistency of U/Pb and ^{40}Ar/^{39}Ar ages amongst several rock types at varying crustal depths indicates that Earth's surface fluids reached significant depth in the Millevaches massif during the Late Carboniferous, as facilitated by synconvergent stretching of the upper crust and coeval high heat flux (which is consistent with previous studies; e.g. Person et al., 2007; Gébelin et al., 2017).

From the samples we have studied in this section, we propose that low δD_{Ms} values from the Millevaches massif were likely acquired between 318.4 ± 1.4 Ma and 309.7 ± 2.3 Ma during coeval high-temperature deformation and meteoric fluid-rock interactions; the age span reflecting the syntectonic growth of mica through time during the shear zone activity (e.g. Gébelin et al., 2011). Calculated δD_{water} values as low as $-104‰$ can be interpreted to reflect a maximum value for meteoric water as the δD_{water} values at the surface may have been potentially lower due to water-rock isotope exchange at depth that inevitably shift the isotope composition of water to more positive values. However, we consider the average of the lowest 30% of the data (δD_{water} value

$= -96 \pm 8‰$; n=3) to represent a conservative estimate for the hydrogen isotopic composition of surface-derived fluids that exchanged with hydrous minerals at depth during high temperature deformation at ∼315 Ma.

4.2. Reconstruction of meteoric water composition in the foreland

By comparison with modern and Jurassic euryhaline sharks (e.g. Dera et al., 2009), we used a phosphate-water isotope exchange temperature of $29 \pm 3°$C (e.g. Fischer et al., 2013) to calculate the oxygen isotopic composition of the fresh water in which the ∼295 Ma-old sharks evolved. Therefore, using the $\delta^{18}O_P$ values obtained from lifelong and short-lived shark proxies (Fischer et al., 2013), and the phosphate-water oxygen fractionation equation (Lécuyer et al., 2013) at a temperature of $29 \pm 3°$C, we calculate $\delta^{18}O_{water}$ values of $-4.1‰$ to $-2.1‰ \pm 0.7‰$ (n=17). We interpret these values to represent the oxygen isotopic composition of fresh water in low-altitude basins during the Late Carboniferous (Table 2). For the paleoaltimetry reconstruction, an average of the lowest 30% of the $\delta^{18}O_{water}$ values of $-3.8 \pm 0.8‰$ (see Table 2 and Figs. 4B and 4C for details and uncertainties) is used to account for potential evaporative enrichment in ^{18}O. This value is consistent with a near-coastal position and low-elevation meteoric water.

4.3. How high was the Limousin region during the Late Carboniferous?

Given the broad range of uncertainties surrounding Carboniferous climate impacts on hydrogen and oxygen isotopes in precipitation, we rely on a comparison of δD_{water} (or $\delta^{18}O_{water}$) at high and low elevation, thus, reducing uncertainties of our paleoaltimetry estimates largely to the uncertainties of the isotopic lapse rate. We, therefore, compare δD values of meteoric water retrieved from ∼315 Ma mylonitic rocks in the hinterland ($\delta D_{water} = -96 \pm 8‰$ or $\delta^{18}O_{water} = -13.3 \pm 1.1‰$) with $\delta^{18}O_{water}$ values calculated from ∼295 Ma freshwater shark remains preserved in the Bourbon l'Archambault foreland basin ($\delta D_{water} = -20 \pm 6‰$ or $\delta^{18}O_{water} = -3.8 \pm 0.8‰$; Figs. 4 and 5).

The difference in δD_{water} values of Late Carboniferous meteoric water between the Felletin detachment mylonites in the hinterland and the Bourbon l'Archambault foreland basin is $\Delta\delta D_{water} = 76 \pm 15‰$ (or $\Delta\delta^{18}O_{water} = 9.5 \pm 1.9‰$). Using a lapse rate of $-22‰$/km for δD_{water} values (e.g. Poage and Chamberlain, 2001), this difference in isotopic compositions indicates an elevation difference of 3.4 ± 0.7 km (Figs. 4 and 5). However, if we use a present-day tropical lapse rate of $-14.6‰$/km (Saylor et al., 2009), we obtain a higher calculated elevation difference of 5.2 ± 1.1 km (Table SM7B). Since we cannot rule out that the time interval of interest in this study was characterized by globally cooler temperatures, 1D-Rayleigh fractionation model lapse rates for mean annual temperatures 5°C lower than today would result in calculated paleoelevation of 3.2 ± 0.5 km (Fig. SM3; see e.g. Jackson et al., 2019).

The error estimate on elevation quantification includes the isotope analyses ($\delta D_{Ms} \pm 2‰$; $\delta^{18}O_P \pm 0.2‰$), the average of the lowest 30% of the isotope ratios ($\delta D_{Ms} \pm 6‰$; $\delta^{18}O_P \pm 0.3‰$) and the temperature estimates (muscovite $\pm 51°$C; sharks $\pm 3°$C), but excludes any uncertainty on the isotope lapse rate, which under present-day conditions attains ca. ± 0.7 km for model elevations of ∼3.4 km (Rowley, 2007).

We hence consider paleoelevations in excess of ∼3 km to represent the preferred estimate for mean paleoelevation of the French Massif Central at ∼315 Ma. It is clear that changes in atmospheric stratification, air mass blocking, evapotranspiration, relative humidity and air parcel trajectories are largely unconstrained but affected isotope lapse rates in the Carboniferous. However, by exploring a range of feasible lapse rates, we feel confident to reliably
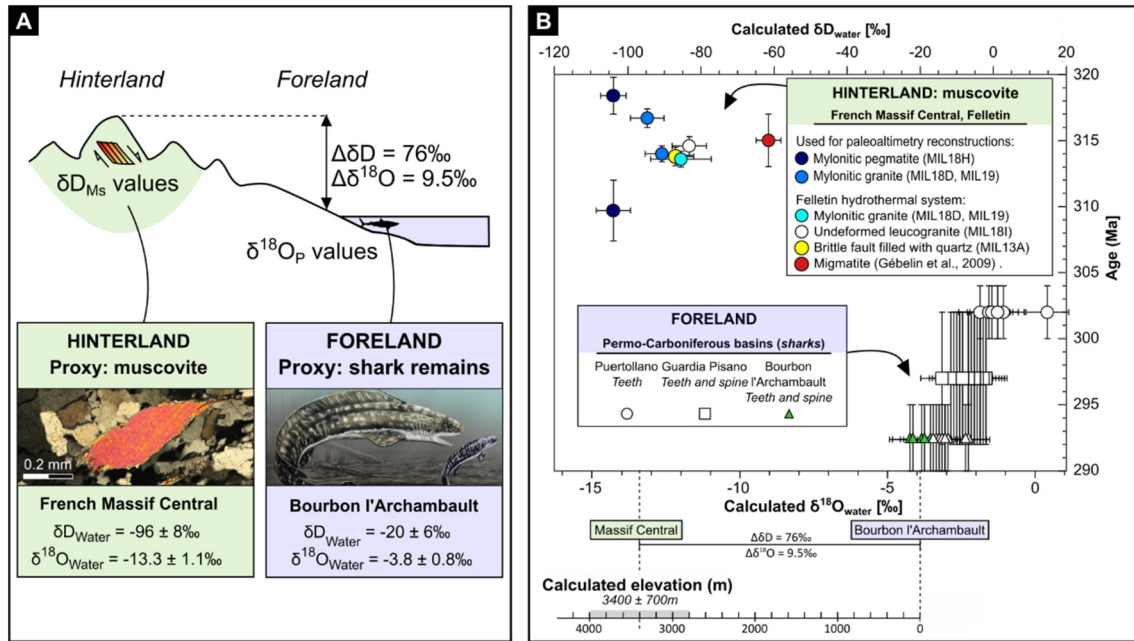
Fig. 5. (A) Schematic cross-section showing the location of proxies and data used for paleoaltimetry reconstructions. (B) δD_{water} values calculated from synkinematic muscovite from the hinterland versus their $^{40}Ar/^{39}Ar$ ages, and $\delta^{18}O_{water}$ values calculated from shark remains in the foreland versus their biostratigraphic and isotopic ages. Difference in $\delta^{18}O_{water}$ values of $\sim$9.5‰ between hinterland proxies (Felletin) and foreland proxies (Bourbon l'Archambault foreland basin) is consistent with Late Carboniferous paleoelevation of the French Massif Central in excess of $\sim$3.0 km (see also Fig. 4). Hydrogen and oxygen isotopes, and geochronological data are detailed in Table SM6. Sharks drawing courtesy of Alain Bénéteau.

provide stable isotope elevation constraints for a segment of one of the largest orogens in Phanerozoic history.

4.4. Assumptions/limitations of paleoaltimetry calculations

Paleoelevation estimates of ca. 3.2-5.2 km calculated using the isotopic composition of ancient rainwater recorded in the hinterland and foreland areas serve as first approximations due to the $\sim$20 Ma age difference between the two proxies ($\sim$315 Ma for mylonites and $\sim$295-290 Ma for sharks).

We consider elevations in excess of $\sim$3 km as robust for the following reasons: First, the average δD_{water} value of -96 ± 8‰ retrieved from the Felletin detachment footwall represents a maximum value as any $\delta D_{meteoric\ water}$ value at the Earth's surface would likely be more negative (e.g. Gébelin et al., 2012). Second, using the lowest δD_{Ms} value of -116‰ obtained from a syntectonic pegmatite (MIL18H), we calculate a δD_{water} value of -104‰ (Table 1) that, reflecting a larger time-integrated meteoric fluid/rock ratio, most closely approximates the isotopic composition of meteoric water at the Earth's surface. Referencing this lowest δD_{water} value to our near sea level record would increase $\Delta\delta D$ to 84‰ and using the lapse rate of Poage and Chamberlain (2001) our paleoelevation estimate to $\Delta z = 3.8 \pm 0.7$ km (Table SM7C). At the same time, the structural position of the sample with the lowest δD_{Ms} value (-116‰; MIL18H) does not follow a simple linear trend of increasing δD_{Ms} values with increasing distance to the detachment (Fig. 3C) suggesting that fluid flow occurred in a localized fashion as has been observed in similar studies (e.g. Gébelin et al., 2011). If we were to exclude this value, our paleoelevation estimates based on the average of the other datapoints would decrease to 3.0 ± 0.7 km as $\Delta\delta D$ decreases to 67‰ (Table SM7D). Third, the Bourbon l'Archambault foreland basin is situated $\sim$100 km from the hinterland sites on the downwind side in the current geographic configuration (Fig. 1). However, the average $\delta^{18}O_{water}$ value of -3.8 ± 0.9‰ obtained from the Bourbon l'Archambault basin is relatively low compared to those calculated from shark remains on the windward side from the Guardia Pisano basin in

Italy (-2.1 ± 0.9‰; n=23; Fig. SM2; Table SM5; Fischer et al., 2013) that would lead to higher paleoelevation estimates of 4.0 ± 0.7 km (Table SM7E). Fourth, an increase of 1.5‰ in $\delta^{18}O_{ocean\ water}$ values (+12‰ in δD) is expected due to storage of low $\delta^{18}O$ ice in the Antarctic ice shield or in continental glaciers (Buggisch et al., 2008).

4.5. Paleoclimatic implications of a moderate-elevation Variscan belt

The Late Paleozoic Ice Age was characterized by voluminous ice sheets in southern Gondwana (e.g. González-Bonorino and Eyles, 1995) and rapid fluctuations between glacial and interglacial conditions (e.g. Michel et al., 2015; Scheffler et al., 2003), with a major glaciation at $\sim$315 Ma (e.g. Montañez and Poulsen, 2013) and peak icehouse conditions at $\sim$298-295 Ma (Soreghan et al., 2019), followed by an increasingly arid Permian climate (e.g. Tabor and Poulsen, 2008). During the Late Carboniferous, the Pangea assemblage moved northward from 10°S to $\sim$5°N between $\sim$315 and $\sim$290 Ma (e.g. Edel et al., 2018; Kent and Muttoni, 2020) and was characterized by a unique and long E-W trending mountain chain, including the French Massif Central (Fig. 1, e.g. Domeier and Torsvik, 2014). This large Paleozoic belt most likely represented an orographic barrier that impacted the transport of air masses mainly coming from the Paleotethys Ocean located to the southeast (Fig. 1; e.g. Fluteau et al., 2001; Tabor and Poulsen, 2008). A comparison with modern conditions suggests that the Variscan mountain range was favorable to high precipitation rates on its southern flank and insulating warm and moist tropical air over the southern Gondwana region from the drier and colder air masses to the north in Laurussia (e.g. Fluteau et al., 2001). Although Laurussia may have been characterized by an orographic rain shadow (e.g. Fluteau et al., 2001), there is evidence for progressive aridification of Laurussia linked to the closure of the Rheic ocean and not to the presence of a mountain chain blocking air masses from the south (e.g. Roscher and Schneider, 2006). However, global atmospheric circulation models simulating paleoclimate of Andean surface uplift indicate that only 50% of the modern Andean plateau

topography (∼2000 m) is sufficient to deflect prevalent air masses from the Pacific ocean, and trigger a South American Low Level Jet where moisture comes from the Equatorial Atlantic (e.g. Insel et al., 2010). Moreover, a rain shadow effect from the Appalachian orogen has been evidenced based on H isotopic analysis of 318-308 Ma clays in the Appalachian Plateau with δD_{water} values down to -72‰ (Boles and van der Pluijm, 2020). Therefore, we propose that even at restrained mean altitude, the Carboniferous Variscan belt of western Europe would have influenced continental moisture transport and associated air mass trajectories.

4.6. How does a medium Variscan mean elevation fit with the Late Carboniferous geological record?

A mean elevation exceeding ∼3 km is in good agreement with the interpretation of the French Massif Central as a segment of thickened crust resulting from the tectonic accretion of Armorica and Gondwana and the closure of the Medio-European ocean (e.g. Matte, 2001). Our results are also consistent with rapid erosion whose products are found in the French Massif Central such as Namurian olistoliths (330-325 Ma), Westphalian turbidites and coarse conglomerates (325-304 Ma) and Stephanian deposits (304-299 Ma) (e.g. Franke and Engel, 1986; Pfeifer et al., 2018). Stephanian basins are usually concentrated in narrow and elongated zones that could be interpreted to reflect the bottom of ancient restricted valleys, reinforcing the presence of an active mountain chain. However, Late Carboniferous-Early Permian coal deposits do not support a very high elevation plateau (e.g. Kent and Muttoni, 2020; Strullu-Derrien et al., 2021). Although the Westphalian and Stephanian deposits support the presence of a topographic high, the activity of detachment zones during the Late Carboniferous indicates that the orogen was collapsing (e.g. Burg et al., 1994; Vanderhaeghe et al., 2020, and references therein).

4.7. Tectonic implications

Although the Variscan belt displays undeniable similarities with the Tibet-Himalaya orogen in its tectonic style and geochemistry of partially molten rocks exhumed in the footwall of detachment faults (e.g. Dörr and Zulauf, 2010), our paleoaltimetry estimates indicate that at ∼315 Ma the French Massif Central region was high but not necessarily similar in its topography to the present-day Himalayan ranges.

Possible explanations include the rheology of the material involved during the mechanisms of deformation during the Paleozoic. Based on the large amount of partially molten rocks, the radioactive heat production of the overthickened crust and the high geothermal gradient, the Variscan belt of western Europe is considered a "hot orogen" where the low viscosity material allows the crust to flow from the hinterland to the foreland (e.g. Vanderhaeghe et al., 2020, and references therein). It is therefore possible that a rather soft and hot crust together with the activity of detachment zones characterizing the Variscan orogen at the end of the orogenic cycle did not support soaring heights, even in the core of the Variscan belt, prior to synorogenic extension. Therefore, our paleoaltimetry estimate exceeding ∼3 km is consistent with the thermal state that characterized this part of the orogen during the Late Carboniferous (e.g. Franke, 2014; Vanderhaeghe et al., 2020). However, our results suggest that the Central Pangea mountain belt was high enough to block air masses from the south-south-east and induce an orographic rainshadow to the north, playing a major role on the Earth's climate at the end of the Carboniferous.

5. Conclusion

Comparison of Late Carboniferous stable isotope multi-proxy records from sites in the internal zone of the Variscan belt (Felletin, French Massif Central) and near sea level (Bourbon l'Archambault basin) allows to quantify the paleoelevation of a major Paleozoic orogen. The low δD values of meteoric water retrieved from ∼315 Ma-old synkinematic hydrous minerals in the Felletin detachment footwall (Millevaches massif) reflect precipitation captured at high (>∼3 km) elevation during the Late Carboniferous. When compared to age-equivalent near-sea level records obtained from freshwater shark remains, differences in $\delta^{18}O_{water}$ and δD_{water} compositions are consistent with minimum elevations of ∼3.4 ± 0.7 km. These results agree with geodynamic models emphasizing the role of partially molten rocks and magmatism in Variscan crustal evolution, reinforcing its characteristic feature of "hot collisional orogen". However, though the Variscan belt of Western Europe cannot be compared from a topographic point of view to the highest modern Himalayan mountains, our paleoaltimetry estimates imply that this orogen represented a major barrier, very likely blocking air masses from the Paleotethys and generating an orographic rain shadow to the north at the end of the Carboniferous.

CRediT authorship contribution statement

Camille Dusséaux: Conceptualization, Data curation, Investigation, Visualization, Writing – original draft. **Aude Gébelin:** Conceptualization, Investigation, Supervision, Writing – original draft. **Gilles Ruffet:** Investigation, Resources, Writing – review & editing. **Andreas Mulch:** Resources, Supervision, Writing – review & editing.

Declaration of competing interest

The authors declare that they have no known competing financial interests or personal relationships that could have appeared to influence the work reported in this paper.

Appendix A. Supplementary material

Supplementary material related to this article can be found online at https://doi.org/10.1016/j.epsl.2021.117064.

References

Alexandrov, P., Ruffet, G., Cheilletz, A., 2002. Muscovite recrystallization and saddle-shaped 40 Ar/ 39 Ar age spectra: example from the Blond granite (Massif Central, France). Geochim. Cosmochim. Acta 66, 1793–1807. https://doi.org/10.1016/S0016-7037(01)00895-X.

Becq-Giraudon, J.-F., Montenat, C., Van Den Driessche, J., 1996. Hercynian high-altitude phenomena in the French Massif Central: tectonic implications. Palaeogeogr. Palaeoclimatol. Palaeoecol. 122, 227–241. https://doi.org/10.1016/0031-0182(95)00081-X.

Blakey, R., 2011. Global paleogeography. NAU Geology. http://www2.nau.edu/rcb7.

Boles, A., van der Pluijm, B., 2020. Locally derived, meteoric fluid infiltration was responsible for Widespread Late Paleozoic Illite Authigenesis in the Appalachian basin. Tectonics 39, e2020TC006137. https://doi.org/10.1029/2020TC006137.

Boos, W.R., Kuang, Z., 2010. Dominant control of the South Asian monsoon by orographic insulation versus plateau heating. Nature 463, 218–222. https://doi.org/10.1038/nature08707.

Buggisch, W., Joachimski, M.M., Sevastopulo, G., Morrow, J.R., 2008. Mississippian δ13Ccarb and conodont apatite δ18O records — their relation to the Late Palaeozoic Glaciation. Palaeogeogr. Palaeoclimatol. Palaeoecol. 268, 273–292. https://doi.org/10.1016/j.palaeo.2008.03.043.

Burg, J.P., Van Den Driessche, J., Brun, J.P., 1994. Syn- to post-thickening extension: mode and consequences. C. R. Acad. Sci., Ser. II Sci. Terre Planet. 319, 1019–1032.

Cartannaz, C., Rolin, P., Cocherie, A., Marquer, D., Legendre, O., Fanning, C.M., Rossi, P., 2007. Characterization of wrench tectonics from dating of syn- to post-magmatism in the north-western French Massif Central. Int. J. Earth Sci. 96, 271–287. https://doi.org/10.1007/s00531-006-0101-y.

Craig, H., 1961. Isotopic variations in meteoric waters. Science 133 (3465), 1702–1703. https://doi.org/10.1126/science.133.3465.1702.

Dera, G., Pucéat, E., Pellenard, P., Neige, P., Delsate, D., Joachimski, M.M., Reisberg, L., Martinez, M., 2009. Water mass exchange and variations in seawater temperature in the NW Tethys during the Early Jurassic: evidence from neodymium and oxygen isotopes of fish teeth and belemnites. Earth Planet. Sci. Lett. 286, 198–207. https://doi.org/10.1016/J.EPSL.2009.06.027.

Domeier, M., Torsvik, T.H., 2014. Plate tectonics in the late Paleozoic. Geosci. Front. 5, 303–350. https://doi.org/10.1016/j.gsf.2014.01.002.

Dörr, W., Zulauf, G., 2010. Elevator tectonics and orogenic collapse of a Tibetan-style plateau in the European Variscides: the role of the Bohemian shear zone. Int. J. Earth Sci. 99, 299–325. https://doi.org/10.1007/s00531-008-0389-x.

Dusséaux, C., Gébelin, A., Boulvais, P., Gardien, V., Grimes, S., Mulch, A., 2019. Meteoric fluid-rock interaction in Variscan shear zones. Terra Nova 31, ter.12392. https://doi.org/10.1111/ter.12392.

Edel, J.B., Schulmann, K., Lexa, O., Lardeaux, J.M., 2018. Late Palaeozoic palaeomagnetic and tectonic constraints for amalgamation of Pangea supercontinent in the European Variscan belt. Earth-Sci. Rev. 177, 589–612. https://doi.org/10.1016/j.earscirev.2017.12.007.

Feulner, G., 2017. Formation of most of our coal brought Earth close to global glaciation. Proc. Natl. Acad. Sci. 114, 11333–11337. https://doi.org/10.1073/pnas.1712062114.

Field, C.W., Fifarek, R.H., 1985. Light stable-isotope systematics in the epithermal environment. In: Berger, B.R., Bethke, P.M. (Eds.), Geology and Geochemistry of Epithermal Systems. Soc. of Econ. Geol., Boulder, Colorado, Colorado, pp. 99–128.

Fischer, J., Schneider, J.W., Voigt, S., Joachimski, M.M., Tichomirowa, M., Tütken, T., Götze, J., Berner, U., 2013. Oxygen and strontium isotopes from fossil shark teeth: environmental and ecological implications for Late Palaeozoic European basins. Chem. Geol. 342, 44–62. https://doi.org/10.1016/j.chemgeo.2013.01.022.

Fluteau, F., Besse, J., Broutin, J., Ramstein, G., 2001. The late Permian climate. What can be inferred from climate modelling concerning Pangea scenarios and Hercynian range altitude? Palaeogeogr. Palaeoclimatol. Palaeoecol. 167, 39–71. https://doi.org/10.1016/S0031-0182(00)00230-3.

Franke, W., 2014. Topography of the Variscan orogen in Europe: failed-not collapsed. Int. J. Earth Sci. 103, 1471–1499. https://doi.org/10.1007/s00531-014-1014-9.

Franke, W., Engel, W., 1986. Synorogenic sedimentation in the Variscan Belt of Europe. Bull. Soc. Géol. Fr. II, 25–33. https://doi.org/10.2113/gssgfbull.II.1.25.

Franke, W., Cocks, L.R.M., Torsvik, T.H., 2017. The Palaeozoic Variscan oceans revisited. Gondwana Research 48, 257–284. https://doi.org/10.1016/j.gr.2017.03.005.

Gébelin, A., Brunel, M., Monié, P., Faure, M., Arnaud, N., 2007. Transpressional tectonics and Carboniferous magmatism in the Limousin, Massif Central, France: structural and 40Ar/39Ar investigations. Tectonics 26. https://doi.org/10.1029/2005TC001822.

Gébelin, A., Jessup, M.J., Teyssier, C., Cosca, M.A., Law, R.D., Brunel, M., Mulch, A., 2017. Infiltration of meteoric water in the South Tibetan Detachment (Mount Everest, Himalaya): when and why? Tectonics 36, 690–713. https://doi.org/10.1002/2016TC004399.

Gébelin, A., Martelet, G., Chen, Y., Brunel, M., Faure, M., 2006. Structure of late Variscan Millevaches leucogranite massif in the French Massif Central: AMS and gravity modelling results. J. Struct. Geol. 28, 148–169. https://doi.org/10.1016/j.jsg.2005.05.021.

Gébelin, A., Mulch, A., Teyssier, C., Heizler, M., Vennemann, T., Seaton, N.C.A., 2011. Oligo-Miocene extensional tectonics and fluid flow across the Northern Snake Range detachment system, Nevada. Tectonics 30, n/a-n/a. https://doi.org/10.1029/2010TC002797.

Gébelin, A., Mulch, A., Teyssier, C., Jessup, M.J., Law, R.D., Brunel, M., 2013. The Miocene elevation of Mount Everest. Geology 41, 799–802. https://doi.org/10.1130/G34331.1.

Gébelin, A., Mulch, A., Teyssier, C., Page Chamberlain, C., Heizler, M., 2012. Coupled basin-detachment systems as paleoaltimetry archives of the western North American Cordillera. Earth Planet. Sci. Lett. 335–336, 36–47. https://doi.org/10.1016/j.epsl.2012.04.029.

Gébelin, A., Roger, F., Brunel, M., 2009. Syntectonic crustal melting and high-grade metamorphism in a transpressional regime, Variscan Massif Central, France. Tectonophysics 477, 229–243. https://doi.org/10.1016/j.tecto.2009.03.022.

Gébelin, A., Teyssier, C., Heizler, M.T., Mulch, A., 2015. Meteoric water circulation in a rolling-hinge detachment system (northern Snake Range core complex, Nevada). Bull. Geol. Soc. Am. 127, 149–161. https://doi.org/10.1130/B31063.1.

Goddéris, Y., Donnadieu, Y., Carretier, S., Aretz, M., Dera, G., Macouin, M., Regard, V., 2017. Onset and ending of the late Palaeozoic ice age triggered by tectonically paced rock weathering. Nat. Geosci. 10, 382–386. https://doi.org/10.1038/ngeo2931.

González-Bonorino, G., Eyles, N., 1995. Inverse relation between ice extent and the late Paleozoic glacial record of Gondwana. Geology 23, 1015. https://doi.org/10.1130/0091-7613(1995)023<1015:IRBIEA>2.3.CO;2.

Heavens, N.G., Mahowald, N.M., Soreghan, G.S., Soreghan, M.J., Shields, C.A., 2015. A model-based evaluation of tropical climate in Pangaea during the late Palaeozoic icehouse. Palaeogeogr. Palaeoclimatol. Palaeoecol. 425, 109–127. https://doi.org/10.1016/j.palaeo.2015.02.024.

Insel, N., Poulsen, C.J., Ehlers, T.A., 2010. Influence of the Andes Mountains on South American moisture transport, convection, and precipitation. Clim. Dyn. 35, 1477–1492. https://doi.org/10.1007/s00382-009-0637-1.

Jackson, L.J., Horton, B.K., Beate, B.O., Bright, J., Breecker, D.O., 2019. Testing stable isotope paleoaltimetry with Quaternary volcanic glasses from the Ecuadorian Andes. Geology 47, 1–4. https://doi.org/10.1130/G45861.1.

Kent, D.V., Muttoni, G., 2020. Pangea B and the Late Paleozoic Ice Age. Palaeogeogr. Palaeoclimatol. Palaeoecol. 553, 109753. https://doi.org/10.1016/j.palaeo.2020.109753.

Lécuyer, C., Amiot, R., Touzeau, A., Trotter, J., 2013. Calibration of the phosphate δ18O thermometer with carbonate–water oxygen isotope fractionation equations. Chem. Geol. 347, 217–226. https://doi.org/10.1016/j.chemgeo.2013.03.008.

Matte, P., 2001. The Variscan collage and orogeny (490-290 Ma) and the tectonic definition of the Armorica microplate: a review. Terra Nova 13, 122–128.

Michel, L.A., Tabor, N.J., Montañez, I.P., Schmitz, M.D., Davydov, V.I., 2015. Chronostratigraphy and Paleoclimatology of the Lodève Basin, France: evidence for a pan-tropical aridification event across the Carboniferous–Permian boundary. Palaeogeogr. Palaeoclimatol. Palaeoecol. 430, 118–131. https://doi.org/10.1016/j.palaeo.2015.03.020.

Miller, C.F., Stoddard, E.F., Bradfish, L.J., Dollase, W.A., 1981. Composition of plutonic muscovite; genetic implications. Can. Mineral. 19, 25–34.

Montañez, I.P., Poulsen, C.J., 2013. The Late Paleozoic Ice Age: an evolving Paradigm. Annu. Rev. Earth Planet. Sci. 41, 629–656. https://doi.org/10.1146/annurev.earth.031208.100118.

Mulch, A., 2016. Stable isotope paleoaltimetry and the evolution of landscapes and life. Earth Planet. Sci. Lett. 433, 180–191. https://doi.org/10.1016/j.epsl.2015.10.034.

Mulch, A., Cosca, M.A., Andresen, A., Fiebig, J., 2005. Time scales of deformation and exhumation in extensional detachment systems determined by high-spatial resolution in situ UV-laser 40Ar/39Ar dating. Earth Planet. Sci. Lett. 233, 375–390. https://doi.org/10.1016/j.epsl.2005.01.042.

Mulch, A., Teyssier, C., Cosca, M.A., Chamberlain, C.P., 2007. Stable isotope paleoaltimetry of Eocene core complexes in the North American Cordillera. Tectonics 26 (4). https://doi.org/10.1029/2006TC001995.

Person, M., Mulch, A., Teyssier, C., Gao, Y., 2007. Isotope transport and exchange within metamorphic core complexes. Am. J. Sci. 307, 555–589. https://doi.org/10.2475/03.2007.01.

Pfeifer, L.S., Soreghan, G.S., Pochat, S., Van Den Driessche, J., Thomson, S.N., 2018. Permian exhumation of the Montagne Noire core complex recorded in the Graissessac-Lodève Basin, France. Basin Res. 30, 1–14. https://doi.org/10.1111/bre.12197.

Poage, M.A., Chamberlain, C.P., 2001. Empirical relationships between elevation and the stable isotope composition of precipitation and surface waters: considerations for studies of paleoelevation change. Am. J. Sci. 301, 1–15. https://doi.org/10.2475/ajs.301.1.1.

Poulsen, C.J., Pollard, D., Montañez, I.P., Rowley, D., 2007. Late Paleozoic tropical climate response to Gondwanan deglaciation. Geology 35, 771. https://doi.org/10.1130/G23841A.1.

Roscher, M., Schneider, J.W., 2006. Permo-Carboniferous climate: Early Pennsylvanian to Late Permian climate development of central Europe in a regional and global context. Geol. Soc. (Lond.) Spec. Publ. 265, 95–136. https://doi.org/10.1144/GSL.SP.2006.265.01.05.

Roscher, M., Schneider, J.W., 2005. An annotated correlation chart for continental Late Pennsylvanian and Permian basins and the marine scale. The Nonmarine Permian. Bull., N. M. Mus. Nat. Hist. Sci. 30, 282–291.

Rowley, D.B., 2007. Stable isotope-based Paleoaltimetry: theory and validation. Rev. Mineral. Geochem. 66, 23–52. https://doi.org/10.2138/rmg.2007.66.2.

Rubio Pascual, F.J., López-Carmona, A., Arenas, R., 2016. Thickening vs. extension in the Variscan belt: P–T modelling in the Central Iberian autochthon. Tectonophysics 681, 144–158. https://doi.org/10.1016/j.tecto.2016.02.033.

Saylor, J.E., Mora, A., Horton, B.K., Nie, J., 2009. Controls on the isotopic composition of surface water and precipitation in the Northern Andes, Colombian Eastern Cordillera. Geochim. Cosmochim. Acta 73, 6999–7018. https://doi.org/10.1016/j.gca.2009.08.030.

Scheffler, K., Hoernes, S., Schwark, L., 2003. Global changes during Carboniferous–Permian glaciation of Gondwana: Linking polar and equatorial climate evo-

lution by geochemical proxies. Geology 31, 605. https://doi.org/10.1130/0091-7613(2003)031<0605:GCDCGO>2.0.CO;2.

Soreghan, G.S., Soreghan, M.J., Heavens, N.G., 2019. Explosive volcanism as a key driver of the late Paleozoic ice age. Geology 47, 600–604. https://doi.org/10.1130/G46349.1.

Stipp, M., Stünitz, H., Heilbronner, R., Schmid, S.M., 2002. The eastern Tonale fault zone: a 'natural laboratory' for crystal plastic deformation of quartz over a temperature range from 250 to 700°C. J. Struct. Geol. 24, 1861–1884. https://doi.org/10.1016/S0191-8141(02)00035-4.

Strullu-Derrien, C., Cleal, C.J., Ducassou, C., Spencer, A.R.T., Stolle, E., Leshyk, V.O., 2021. A rare late Mississipian flora from Northwestern Europe (Maine-et-Loire Coalfield, Pays de la Loire, France). Rev. Palaeobot. Palynol. 285, 104359. https://doi.org/10.1016/j.revpalbo.2020.104359.

Suzuoki, T., Epstein, S., 1976. Hydrogen isotope fractionation between OH-bearing minerals and water. Geochim. Cosmochim. Acta 40, 1229–1240. https://doi.org/10.1016/0016-7037(76)90158-7.

Tabor, N.J., Poulsen, C.J., 2008. Palaeoclimate across the Late Pennsylvanian–Early Permian tropical palaeolatitudes: a review of climate indicators, their distribution, and relation to palaeophysiographic climate factors. Palaeogeogr. Palaeoclimatol. Palaeoecol. 268, 293–310. https://doi.org/10.1016/j.palaeo.2008.03.052.

Taylor, H.P., 1977. Water/rock interactions and the origin of H_2O in granitic batholiths. J. Geol. Soc. (Lond.) 133, 509–558. https://doi.org/10.1144/gsjgs.133.6.0509.

Vanderhaeghe, O., Laurent, O., Gardien, V., Moyen, J.-F., Gébelin, A., Chelle-Michou, C., Couzinié, S., Villaros, A., Bellanger, M., 2020. Flow of partially molten crust controlling construction, growth and collapse of the Variscan orogenic belt: the geologic record of the French Massif Central. BSGF - Earth Sci. Bull. https://doi.org/10.1051/bsgf/2020013.

Wu, C.-M., Chen, H.-X., 2015. Calibration of a Ti-in-muscovite geothermometer for ilmenite- and Al2SiO5-bearing metapelites. Lithos 212–215, 122–127. https://doi.org/10.1016/j.lithos.2014.11.008.

Further reading

Mulch, A., Chamberlain, C.P., 2007. Stable isotope paleoaltimetry in orogenic belts – The silicate record in surface and crustal geological archives. Rev. Mineral. Geochem. 66, 89–118. https://doi.org/10.2138/rmg.2007.66.4.